The Astrophysical Journal, 773:22 (11pp), 2013 August 10 doi:10.1088/0004-637X/773/1/22

CENTAURS AND SCATTERED DISK OBJECTS IN THE THERMAL INFRARED: ANALYSIS OF *WISE*/*NEOWISE* OBSERVATIONS

James M. Bauer[1,2], Tommy Grav[3], Erin Blauvelt[1], A. K. Mainzer[1], Joseph R. Masiero[1], Rachel Stevenson[1], Emily Kramer[1,4], Yan R. Fernández[4], C. M. Lisse[5], Roc M. Cutri[2], Paul R. Weissman[1], John W. Dailey[2], Frank J. Masci[2], Russel Walker[6], Adam Waszczak[7], Carrie R. Nugent[1], Karen J. Meech[8,9], Andrew Lucas[2], George Pearman[2,10], Ashlee Wilkins[1,11], Jessica Watkins[12], Shrinivas Kulkarni[13], Edward L. Wright[14]
and the WISE and PTF Teams
[1] Jet Propulsion Laboratory, California Institute of Technology, 4800 Oak Grove Drive, MS 183–401, Pasadena, CA 91109, USA; bauer@scn.jpl.nasa.gov
[2] Infrared Processing and Analysis Center, California Institute of Technology, Pasadena, CA 91125, USA
[3] Planetary Science Institute, 1700 East Fort Lowell, Suite 106, Tucson, AZ 85719–2395, USA
[4] Department of Physics, University of Central Florida, 4000 Central Florida Boulevard, P.S. Building, Orlando, FL 32816–2385, USA
[5] Applied Physics Laboratory, Johns Hopkins University, 11100 Johns Hopkins Road, Laurel, MD 20723–6099, USA
[6] Monterey Institute for Research in Astronomy, 200 Eighth Street, Marina, CA 93933, USA
[7] Division of Geological and Planetary Sciences, California Institute of Technology, Pasadena, CA 91125, USA
[8] Institute for Astronomy, University of Hawaii, 2680 Woodlawn Drive, Manoa, HI 96822, USA
[9] NASA Astrobiology Institute, Institute for Astronomy, University of Hawaii, Manoa, HI 96822, USA
[10] University of California, Berkeley, CA, USA
[11] Department of Astronomy, University of Maryland, College Park, MD 20742–2421, USA
[12] Institute for Planets and Exoplanets, University of California, 3713 Geology, 595 Charles Young Drive East, Los Angeles, CA 90095, USA
[13] Division of Mathematics, Physics, and Astronomy, California Institute of Technology, Pasadena, CA 91125, USA
[14] Department of Physics and Astronomy, University of California, PO Box 91547, Los Angeles, CA 90095–1547, USA
Received 2013 February 23; accepted 2013 June 5; published 2013 July 22

ABSTRACT

The *Wide-field Infrared Survey Explorer* (*WISE*) observed 52 Centaurs and scattered disk objects (SDOs) in the thermal infrared, including 15 new discoveries. We present analyses of these observations to estimate sizes and mean optical albedos. We find mean albedos of 0.08 ± 0.04 for the entire data set. Thermal fits yield average beaming parameters of 0.9 ± 0.2 that are similar for both SDO and Centaur sub-classes. Biased cumulative size distributions yield size–frequency distribution power law indices of $\sim -1.7 \pm 0.3$. The data also reveal a relation between albedo and color at the 3σ level. No significant relation between diameter and albedos is found.

Key words: comets: general – minor planets, asteroids: general

Online-only material: color figures

1. INTRODUCTION

The region of the outer solar system between the giant planets is a dynamically unstable domain for small body orbits. The cometary and asteroidal bodies that spend the majority of their time in this region, the Centaurs, typically have dynamical lifetimes of only tens of millions of years (cf. Holman & Wisdom 1993; Horner et al. 2004). Centaurs form a link between the more distant populations, such as the scattered disk objects (SDOs) and trans-Neptunian objects (TNOs) with populations that reside closer in toward the Sun, such as the Jupiter Family Comets (JFCs) and Near-Earth Comets.

As the transition stage between the TNO reservoir of bodies (Gladman et al. 2008) that evolve to become inner system JFCs, Centaurs (Horner et al. 2004), and SDOs (Gladman et al. 2008; Elliot et al. 2005) serve as a means of transport of volatiles to the terrestrial planets and inner solar system. The diversity of observable properties in the JFC population (A'Hearn et al. 1995; Schleicher et al. 2012; Fernández et al. 2013; Kelley et al. 2013) and this population's variances in behavior and gas species abundances (Bauer et al. 2011; 2012a, 2012a, 2012b) may be demonstrative of evolutionary processes, or may be intrinsic properties related to formation distances.

Whether evolutionary effects are manifest in the reservoir populations (Brown 2000; Lamy et al. 2001; Jewitt 2004) or whether the differences in the observable surface properties of these populations, for example in color (Tegler et al. 2008, and references therein), are linked to primordial compositional variations has not been definitively determined. The albedos (p_v) of JFCs, 0.04 ± 0.02 (Fernández et al. 2013), are on average less than the observed albedos for SDOs and Centaurs (as detailed below). Should color be linked to albedo, these properties may trace the surface volatile content, and thus the age and evolution of these bodies (cf. Jewitt 2009; Fraser & Brown 2012; Lisse et al. 2013).

Numerous schemes have been proposed for the classification and nomenclature of outer solar system bodies (cf. Horner et al. 2004; Elliot et al. 2005; Delsanti & Jewitt 2006; Gladman et al. 2008). All are primarily founded on arguments concerning the dynamical evolution of the related objects. However, owing to the distance of these bodies, the pace of their physical characterization has been ponderous. In most cases, large-aperture telescopes are necessary to make accurate photometric and spectro-photometric observations (cf. Bauer et al. 2003; Delsanti et al. 2006; Tegler et al. 2008). Even the most basic physical property, size, has remained elusive because the surface-reflectances and colors of these objects can vary by factors of several (Jewitt & Kalas 1998; Fernández et al. 2002; Barucci et al. 2008), leading to sizes based on reflected light having commensurately large uncertainties. With the advent of space-based thermal infrared observations with the *Spitzer Space Telescope* (*Spitzer*; Werner et al. 2004), the derivation of sizes for many of these bodies became possible. Prior to *Spitzer*, only a handful of outer solar system bodies had measured

diameters in the literature (Fernández et al. 2002). The work of Stansberry et al. (2008) demonstrated the effectiveness of such thermal IR observations by providing diameters for 47 of these objects and setting constraints on surface reflectance and thermal beaming parameters, which indicate the degree to which the small body's emission deviates from that of an idealized sphere in instantaneous thermal equilibrium (Harris 1998). The data set was large enough to make comparisons that were statistically meaningful with respect to dynamical subclasses, but indicated at best only weak relationships between the subclasses. Recently, the *Herschel* spacecraft, too, has sampled 15 SDOs (Santos-Sanz et al. 2012, hereafter S12). Both S08 and S12 have some overlap with the *WISE* sample of objects.

The *WISE* mission surveyed the entire sky at four mid-IR wavelengths simultaneously: 3.4 μm ($W1$), 4.6 μm ($W2$), 12 μm ($W3$), and 22 μm ($W4$), with greatly improved sensitivity and resolution over previous surveys at these wavelengths (Wright et al. 2010). The field of view for each *WISE* exposure was 47 arcmin on a side, with a pixel scale of 2.75 arcsec pixel^{-1}. Each point on the sky was observed an average of 12 times, with depth of coverage increasing toward the ecliptic poles (Cutri et al. 2012). For this paper we have utilized the *NEOWISE* enhancements to the *WISE* data processing system (Mainzer et al. 2011a), which provided a solar system object archive and a moving object detection algorithm. The *WISE* Moving Object Processing Software (WMOPS; Dailey et al. 2010; Mainzer et al. 2011a) successfully found a wide array of primitive bodies detected by *WISE*, including Near-Earth Objects (NEOs), main belt asteroids, comets, and Trojan and Centaur asteroids. By the end of the spacecraft mission, *NEOWISE* identified more than 158,000 small bodies, including 155 comets (cf. Mainzer et al. 2011a; Bauer et al. 2012b) and 157,000 asteroids (Masiero et al. 2011). The archive augmentation identifies all the *WISE* observations that covered the predicted positions of moving objects. Many of the Centaurs and SDOs were found over the course of the mission by WMOPS, but a large fraction of the fainter Centaurs were found by stacking the images that were identified as covering the particular Centaur in question using the archive service.

For asteroids and cometary nuclei, the *WISE* observations were found to be useful for determining solid body size and albedo distributions, and thermo-physical properties such as thermal inertia, the magnitude of non-gravitational forces, and surface roughness (Mainzer et al. 2011b, 2011c; Bauer et al. 2012c; Nugent et al. 2012). The intended scope of this paper is to present the thermal fits of the Centaurs and SDOs and their immediate interpretation. The sample is not de-biased. Many of the detections of the bodies were from stacked images, and sensitivity was greatly affected by object distance and size, rate of apparent motion, and surface reflectance. For the objects detected through stacking, their selection biases depend on the circumstances of their discovery, usually by ground-based surveys searching at visible wavelengths. Such surveys are intrinsically biased against lower albedo objects. Thus, the combined survey biases of the Centaur and SDO sample in this paper consist of a mix of the infrared/WMOPS-selected sample as well as the visual-wavelength-selected sample detected through stacking. De-biasing the observed population, and the interpretation of the de-biasing with respect to the underlying populations, will be covered in a paper soon to follow.

All objects we discuss reside primarily within or cross through the region of the giant planet orbits and have semi-major axes, a, beyond the orbit of Jupiter, so that in the broadest definition (cf. Levison & Duncan 1997) they may be considered Centaurs. A similar definition for Centaurs is employed by the JPL solar system dynamics node (http://ssd.jpl.nasa.gov) for all objects with 5.5 AU $< a <$ 30.1 AU. We do not impose nomenclature on our subsets, and list the orbital elements (eccentricity, e, semi-major axis, a (AU), and inclination, i (°)) for the reader's interpretation (see Table 4). However, the definition of a Centaur is not rigid (Davies et al. 2008; Horner et al. 2004), and other combinations of orbital parameters have been used to define or sub-divide this class of objects (Gladman et al. 2008), including that Centaurs be required to have a $q > 5.2$ AU (cf. Tegler et al. 2008; Jedicke et al. 2002). For the purposes of our discussion, we do utilize a working definition, without formal explanation, of a subclass of Centaur objects with perihelion distance, $q < 5.2$ AU, and $a > 5.5$ AU, calling them "Satyrs," in order to differentiate between the two classification schemes above. Those objects with aphelion distance $Q > 35$ AU are categorized as SDOs, as they satisfy the criterion described in Elliot et al. (2005) with $T_N < 3$ (Table 4) identified with the population of scattered objects indicated in Duncan & Levison (1997).

2. OBSERVATIONS AND ANALYSIS

2.1. Shorter Wavelength Observations

The *WISE* thermal observations provide an effective means of determining the size and beaming parameters for small bodies in general, and the Centaurs and SDOs in our observed sample (see Section 2.2). However, the reflected-light signal for most bodies was completely unconstrained by the *WISE* observations. For all 52 objects observed, the mean of the object heliocentric distances (R_h) at the time of observation was 10.5 AU, and only 10 of these were detected at $R_h < 5$ AU, while only one was observed at $R_h < 2$ AU.

The strength of the signal in each band is determined by a number of factors including R_h, phase angle, diameter, surface temperature, surface roughness, rotation rate, and surface reflectance. Since many of these factors were not previously measured, it was difficult to predict with certainty which bodies would have detectable flux in specific bands. A general relationship between R_h (in AU) and the wavelength of peak emission, λ_{peak} (in μm), can be derived by using Wien's law and assuming the sub-solar temperature, $T_{ss} \sim 394\ \mathrm{K} \cdot \sqrt{R_h}$, dominates the signal, such that:

$$R_h \approx \left(\frac{\lambda_{peak}}{7.35}\right)^2. \quad (1)$$

In general, using this expression for a slowly rotating small body with low surface-reflectance, the sub-solar temperature would produce a peak flux at a wavelength longward of the $W2$ bandpass when the object is at a distance of $R_h \sim 0.6$ AU. Similarly, the peak flux would fall longward of $W3$ at $R_h > 4$ AU, and longward of $W4$ at $R_h > 10$ AU. Using a more sophisticated thermal model (Section 2.2) in combination with the expected reflected-light signal, the thermal signal would exceed the reflected-light out to distances of $R_h \sim 4$ AU for $W2$, and $R_h \sim 15$ AU for $W3$. Folding in the estimated signal-to-noise in each band as reported in Wright et al. (2010), the signal-to-noise ratio (S/N) would be greatest in $W2$ out to $R_h \sim 1$ AU, and in $W3$ from $R_h \sim 1$ to 2.3 AU. Beyond $R_h \sim 2.3$ AU, the S/N would be greatest in $W4$, with the idealized case of $p_V \sim 0.04$ and a slowly rotating body.

Only 5 out of the 52 outer solar system small bodies detected by *WISE* had significant signals in *W*1 or *W*2, even after stacking: Chiron, 2010 OR_1, 2010 LG_{61}, 2008 SO_{218}, and 2008 YB_3 (see Table 1). Owing to possible compositional variation in these bodies, *W*1 and *W*2 are not readily convertible to reflected-light *V*-band magnitudes. We therefore utilized our visual-band measurements and visual-band measurements from the literature in our fits to constrain p_V. All objects had estimates of absolute magnitude, $H_v(1,1,0)$, based on discovery and astrometric observation reports provided by the Minor Planet Center (MPC; http://www.minorplatencenter.net). Errors on the *H* magnitudes were taken to be ±0.3 mag in cases where only MPC data was available following Mainzer et al. (2011a) and Masiero et al. (2011); it should be noted that considerable uncertainty about the catalog *H* and phase curve slope parameter *G* values exists (cf. Pravec et al. 2012). However, in order to classify a significant sample as to their Centaur color class (Tegler et al. 2008), we observed a subset of our Centaur/SDO targets from ground-based telescopes (Table 2) and used photometry from the literature where otherwise available (Table 3). A total of 33 Centaurs and SDOs of the 52 *WISE* objects observed have colors measured in this fashion. We also augmented our sample with eight bodies with measured diameters and color photometry from Stansberry et al. (2008, hereafter S08), so that our total sample for comparative analysis included 60 objects. Table 3 lists the references of known colors and $B-R$ values used in our data analysis.

Over the course of the *WISE* mission, and the three observing semesters immediately following, the *NEOWISE* team used ground-based telescopes to obtain visual-band and NIR observations of small-body targets. Time at the SOAR 4 m and Palomar 200 inch telescopes was used to obtain *B* and *R* Bessel-filter photometry (Bessell 1990) of the Centaurs and SDOs in our sample. We list the observed *R*-band magnitude, and $B-R$ values found from our observations in Table 2, as well as the dates and site information. Most of these objects do not have well-constrained phase curve behavior. We also bracketed the *B*-band observations by *R*-band observations, but we found no significant *R*-band variation owing to rotation or cometary activity over the course of our observations. In most cases, the ground-based exposures spanned less than 40 minutes in total for each object.

2.2. Thermal Observations

The *WISE* spacecraft surveyed the entire sky as its terminator-following polar orbit around the Earth progressed about 1 degree of ecliptic longitude per day. Regular survey operations commenced on 2010 January 14 (MJD 55210), imaging the sky simultaneously in all four photometric bands until the solid hydrogen cryogen was depleted in the secondary tank on 2010 August 6 UTC (MJD 55414). The survey then entered a three-band (*W*1–*W*3) phase that lasted through 2010 September 29 UTC (MJD 55469). The final phase, the post-cryogenic mission with only *W*1 and *W*2 operating, lasted from through 2011 February 1 (MJD 55593; cf. Cutri et al. 2012). All photometric data of detected objects presented here were obtained during the cryogenic phase.

During the fully cryogenic portion of the mission, simultaneous exposures in the four *WISE* wavelength bands were taken once every 11 s, with exposure durations of 8.8 s in *W*3 and *W*4, and 7.7 s in *W*1 and *W*2 (Wright et al. 2010). The number of exposures acquired on each moving object varied depending on the location of the object on the sky, especially its ecliptic latitude, the toggle pattern of the survey employed to avoid imaging the Moon, and the relative motion of the object with respect to the progression of the survey (Mainzer et al. 2011a; Cutri et al. 2012). Note that *WISE* may have observed a moving solar system object while it was in different patches of the sky, i.e., when several weeks or months had passed since the previous exposure (e.g., comet 67P; Bauer et al. 2012a); henceforth, we refer to the series of exposures containing the object in the same region of sky as a "visit." The spatial resolution in the *WISE* images varies with the wavelength of the band. The FWHM of the mean point-spread-function (PSF), in units of arcseconds was 6.1, 6.4, 6.5, and 12.0 for *W*1, *W*2, *W*3, and *W*4, respectively (Wright et al. 2010; Cutri et al. 2012).

Like the comets we have previously studied (Bauer et al. 2011, 2012a, 2012c), the analysis of the Centaurs and SDOs often required stacking to obtain reliable S/Ns. For each body, the images were identified using the *WISE* image server (http://irsa.ipac.caltech.edu/applications/wise), as described by Cutri et al. (2012), and were stacked using the moving object routine, "A *WISE* Astronomical Image Co-adder" (AWAIC; Masci & Fowler 2009). The images were stacked to both boost the S/N in the thermal bands and to average over any rotational variations in the signals. The ∼10–12 observations per object span ∼36 hr for most objects, which is probably a reasonable averaging over most Centaur rotational periods, which are shorter than 27 hr (cf. Rousselot et al. 2005) and in most cases <11 hr (cf. Bauer et al. 2002, 2003; Ortiz et al. 2002, 2003; Thirouin et al. 2010). As the objects were not generally observed at heliocentric distances (R_h) of less than 4 AU, most objects were brightest in *W*4, and only four had any unambiguous reflected-light signal at shorter wavelengths (*W*1 and *W*2; see Section 1). Figure 1 shows the distribution of the Centaurs and SDOs as a function of R_h and indicates a paucity of

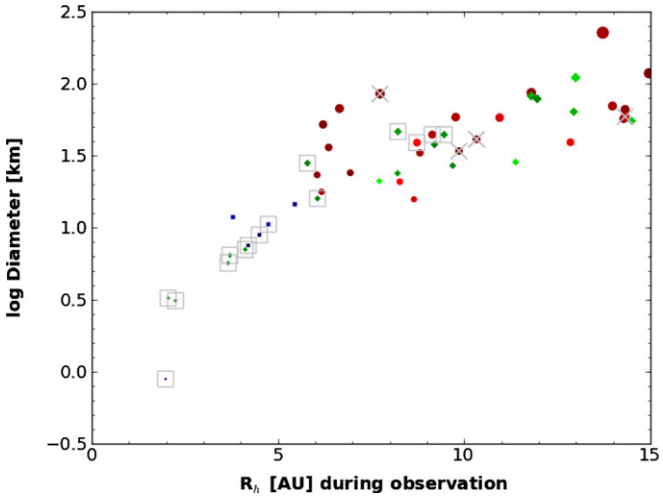

Figure 1. Log of the fitted diameter as compared to the heliocentric distance at the time of observations for 44 of the objects in our survey, plus four from S08 and Tegler et al. (2008). Symbols are color-coded as SDOs (green diamonds), Centaurs (red circles), and the Centaur sub-population of "Satyrs" (blue squares) with $q < 5.2$. The log value of the fitted diameter is also represented by the size of the symbol. The relative visual-band albedo is shown approximately as the darkness of the symbol. Those symbols with boxes around them indicate the objects discovered by *NEOWISE*, and those with an "X" through them represent the supplemented known objects not detected by *WISE*, but with measured diameters and colors reported in Stansberry et al. (2008) and Tegler et al. (2008).

(A color version of this figure is available in the online journal.)

Table 1
Extracted Fluxes of Centaurs and SDOs

Object[a]	MPC Designation[1]	H_V[a]	R_h[a] (AU)	Δ[a] (AU)	α[a]	$W3$ (mJy)	$W4$ (mJy)	$W1$ (mJy)	$W2$ (mJy)
10199	(10199) Chariklo	6.66	13.75	13.72	4.1	0.5 ± .1	52 ± 5	...	...
167P	167P/CINEOS	9.7	14.31	14.28	4.1	...	5 ± 1	...	...
2060	(2060) Chiron	6.5	16.31	16.28	3.6	0.30 ± .06	24 ± 3	...	0.08 ± .01
29P[b]	29P/Schwassmann-Wachmann 1	9.	6.21	6.04	9.3	18 ± 3	144 ± 23	...	...
31824	(31824) Elatus	10.1	14.28	14.15	4.0	...	4 ± 1	...	...
32532	(32532) Thereus	9.	11.8	11.67	4.8	0.19 ± .03	6.0 ± .1	.11 ± .03	.14 ± .03
42355	(42355) Typhon	7.5	18.08	17.96	3.2	...	4 ± 1	...	...
52872	(52872) Okyrhoe	11.	6.72	6.54	8.7	2.9 ± .3	42 ± 4	...	...
52872	(52872) Okyrhoe	11.	6.44	6.35	8.8	3.5 ± .4	47 ± 4	...	...
54598	(54598) Bienor	7.5	17.37	17.33	3.4	0.05 ± .01	11 ± 1	...	...
55576	(55576) Amycus	7.46	16.72	16.69	3.4	...	5 ± 1	...	...
60558	(60558) Echeclus	9.55	9.77	9.71	5.8	1.5 ± .3	32 ± 5	...	...
60558	(60558) Echeclus	9.55	9.32	9.17	6.2	1.8 ± .3	37 ± 5	...	...
95626	(95626) 2002 GZ32	7.	19.12	19.11	2.9	...	15 ± 2	...	...
95626	(95626) 2002 GZ32	7.	19.02	18.92	3.0	...	15 ± 1	...	...
C0061	(120061) 2003 CO1	8.9	11.80	11.76	4.8	0.4 ± .1	19 ± 2	...	...
C7546	(127546) 2002 XU93	7.9	21.06	20.95	2.7	...	2.5 ± .4	...	...
CK11K36P	C/2011 KP36 (Spacewatch)	9.4	14.54	14.51	3.9	...	3.3 ± .7	...	...
D6204	(136204) 2003 WL7	8.6	14.98	14.85	3.8	...	9 ± 2	...	...
E5486	(145486) 2005 UJ438	10.5	8.27	8.14	6.9	0.5 ± .1	4 ± 1	...	...
E8975	(148975) 2001 XA255	11.2	9.37	9.25	6.0	...	11 ± 4	...	...
E8975	(148975) 2001 XA255	11.2	9.34	9.21	6.2	0.8 ± .2	15 ± 3	...	...
K05VB9J	2005 VJ119	10.6	11.51	11.37	5.0	...	2.5 ± .5	...	...
K05VB9J	2005 VJ119	10.6	11.38	11.31	5.0	...	3.2 ± .8	...	...
K07VU5H	2007 VH305	8.21	8.21	8.09	6.9	1.0 ± .2	6 ± 1	...	...
K08H21Y	2008 HY21	12.1	6.94	6.86	8.3	0.6 ± .1	12 ± 2	...	...
K08J14S	2008 JS14	13.2	5.45	5.28	10.4	1.4 ± .4	14 ± 3	...	...
K10B04L	2010 BL4	11.9	8.65	8.49	6.6	...	3.1 ± .8	...	...
K10BB8K	2010 BK118	10.2	8.22	8.09	6.7	1.9 ± .2	33 ± 5	...	...
K10CE0R	2010 CR140	15.5	4.20	4.04	13.6	1.6 ± .1	10 ± 1	...	...
K10E65S	2010 ES65	11.8	9.69	9.56	6.0	0.30 ± .07	5.4 ± .9	...	...
K10F92H	2010 FH92	11.7	5.79	5.70	9.9	7.5 ± .5	60 ± 4	...	...
K10G64W	2010 GW64	14.9	3.71	3.50	15.6	4.2 ± .4	16 ± 2	...	...
K10GE7W	2010 GW147	13.2	6.09	6.01	9.5	1.2 ± .1	12.6 ± 0.9	...	...
K10H20U	2010 HU20	13.0	4.74	4.63	12.2	1.9 ± .3	13 ± 2	...	...
K10JC4H	2010 JH124	14.6	4.13	3.93	14.1	2.1 ± .3	11 ± 2	...	...
K10K07W	2010 KW7	15.5	3.00	2.74	19.6	5.7 ± .5	17 ± 2	...	...
K10L61G	2010 LG61	18.5	1.57	1.21	40.3	3.6 ± .5	8 ± 3	...	...
K10O01R	2010 OR1	16.2	2.78	2.54	20.7	4.2 ± .5	12 ± 2	0.41 ± .03	...
K10OA1M	2010 OM101	17.	2.25	2.01	26.8	7.7 ± .8	19 ± 3	...	...
K10P58O	2010 PO58	14.5	4.50	4.33	13.0	2.1 ± .2	13 ± 2	...	...
K10R64M	2010 RM64	11.0	7.79	7.71	7.5	0.46 ± .09	8 ± 2	...	...
K10T00H	2010 TH	9.2	13.99	13.96	4.2	...	7 ± 1	...	...
K10W09G	2010 WG9	8.1	19.33	19.24	2.9	...	2.9 ± .3	...	...
K11M04M	2011 MM4	9.3	12.94	12.90	4.4	0.11 ± .02	7.3 ± .7	...	...
O8835	(248835) 2006 SX368	9.5	11.96	11.91	4.9	0.6 ± .2	18 ± 2	...	...
P0112	(250112) 2002 KY14	9.5	8.73	8.69	6.7	1.2 ± .2	22 ± 3	...	...
S1371	(281371) 2008 FC76	9.1	10.95	10.89	5.3	0.8 ± .1	21 ± 2	...	...
U9139	(309139) 2006 XQ51	9.8	12.85	12.73	4.4	...	3.0 ± .7	...	.....
U9737	(309737) 2008 SJ236	12.2	6.60	6.44	8.6	1.1 ± .2	13 ± 2	...	...
V0071	(310071) 2010 KR59	7.7	13.00	12.85	4.4	...	22 ± 3	...	...
W8884	(328884) 2010 LJ109	10.1	9.14	8.99	6.4	1.0 ± .2	21 ± 3	...	...
X0759	(330759) 2008 SO218	12.8	3.70	3.57	15.9	12 ± 1	52 ± 5	...	...
X2685	(332685) 2009 HH36	10.6	8.02	7.71	6.8	1.3 ± .2	22 ± 3	...	...
X6756	(336756) 2010 NV1	10.5	9.45	9.42	6.2	1.0 ± .3	21 ± 5	...	...
Y2842	(342842) 2008 YB3	9.5	6.65	6.51	8.7	14 ± 1	171 ± 10	0.16 ± .02	...
Y6889	(346889) 2009 QV38	11.8	6.05	5.95	9.6	3.2 ± .5	...	...	...

Notes.
[a] Object name in packed-provisional format (http://www.minorplanetcenter.org/iau/info/PackedDes.html). The MPC Designation is the full designation as specified in the Minor Planet Center's one-line format ephemeris output for the object. H_V: solar-system absolute magnitude; R_h: heliocentric distance of object at time of observation in AU; Δ: object–spacecraft distance at time of observation in AU. α: Sun–object–spacecraft (phase) angle in degree units.
[b] Preliminary coma-extracted fluxes for 29P are provided here (see text).

Table 2
New Centaur and SDO Colors

Object	Date (UT)	Telescope/Instrument	m_R	$B-R$
CK36P	2012 Mar 27	Pal. 200in/LFC	20.88 ± .08	1.42 ± .10
E5486	2012 Mar 21	SOAR/SOI	20.92 ± .04	1.55 ± .05
K07VU5H	2012 Sep 19	Pal. 200in/LFC	20.14 ± .01	2.27 ± .09
K10 BB8K	2012 Jul 10	Pal. 200in/LFC	18.27 ± .02	1.29 ± .02
K10B41L	2012 Mar 21	SOAR/SOI	21.57 ± .11	1.09 ± .14
K10F92H	2010 Apr 18	SOAR/SOI	19.22 ± .03	1.30 ± .05
K10GE7W	2012 Mar 27	Pal. 200in/LFC	23.20 ± .10	0.95 ± .14
K10R64M	2012 Mar 21	SOAR/SOI	18.52 ± .02	2.24 ± .05
O8835	2012 Sep 19	Pal. 200in/LFC	20.17 ± .03	1.28 ± .14
P0112	2012 Sep 19	Pal. 200in/LFC	19.34 ± .03	1.69 ± .04
S1371	2012 Sep 19	Pal. 200in/LFC	19.18 ± .03	1.52 ± .07
V0071	2012 Mar 21	SOAR/SOI	20.91 ± .12	1.59 ± .12
V8884	2012 May 26	Pal. 200in/LFC	19.73 ± .03	1.19 ± .17
X0759	2012 Mar 21	SOAR/SOI	20.98 ± .04	1.50 ± .10
X2685	2012 Mar 21	SOAR/SOI	19.84 ± .03	1.10 ± .04
X6756	2012 Jul 10	Pal. 200in/LFC	20.42 ± .10	1.20 ± .14
Y6889	2012 Dec 12	Pal. 200in/LFC	20.75 ± .04	1.15 ± .14

Table 3
Known Centaur Colors

Object	Reference	$B-R$
10199	Tegler et al. 2008	1.26 ± .04
10370	Tegler et al. 2008	1.15 ± .06
167P	Jewitt 2009	1.30 ± .05
2060	Tegler et al. 2008	1.04 ± .05
29P	Jewitt 2009	1.28 ± .04
31824	Tegler et al. 2008	1.70 ± .02
32532	Tegler et al. 2008	1.18 ± .01
42355	Peixinho et al. 2012	1.29 ± .07
5145	Tegler et al. 2008	2.04 ± .07
52872	Tegler et al. 2008	1.21 ± .02
52975	Tegler et al. 2008	1.86 ± .05
54598	Tegler et al. 2008	1.12 ± .03
55576	Tegler et al. 2008	1.79 ± .03
60558	Tegler et al. 2008	1.38 ± .04
63252	Tegler et al. 2008	1.20 ± .03
7066	Tegler et al. 2008	1.88 ± .06
83982	Tegler et al. 2008	1.85 ± .02
8405	Tegler et al. 2008	1.23 ± .05
95626	Tegler et al. 2008	1.03 ± .04
C0061	Tegler et al. 2008	1.24 ± .04
C7546	Hainaut et al. 2012	1.20 ± .03
D6204	Peixinho et al. 2012	1.23 ± .04
E8975	Fraser & Brown 2012	1.23 ± .10[a]
Y2842	Sheppard 2010	1.26 ± .01

Notes. [a] $B-R$ color extrapolated from *Hubble Space Telescope*'s Wide-Field Camera 3 observations through the $F606w$ and $F814w$ filters.

small-diameter objects at large heliocentric distances, a biasing artifact of the spacecraft's sensitivity limits in the thermal bands (particularly $W4$), as well as the visual-wavelength discovery selection bias for the objects recovered in the stacked images. Table 1 shows the extracted flux values for the stacked images and viewing geometries, including phase angles.

We used the thermal model developed specifically for solar system objects in the *WISE* data described in Mainzer et al. (2011b). This model is an adaptation of the Near-Earth asteroid thermal model (NEATM; Harris 1998). Counts are converted to in-band magnitudes and uncertainties using aperture photometry count values from stacked images and applying the $W1$–$W4$ zero-point offsets in Wright et al. (2010). The magnitudes require color-corrections based on each object's temperature when converting them into flux densities. These corrections are typically small for $W4$, on the order of a few percent. For $W3$, however, these can be several tens of percent, though the corrections are well-characterized (Mainzer et al. 2011b; Wright et al. 2010), yielding flux uncertainties on the order of 5%–10%. As discussed in Mainzer et al. (2011b), the thermal model converts raw instrumental magnitudes into monochromatic flux densities using the color corrections outlined in detail in Wright et al. (2010), deriving an effective temperature for this conversion based on the object's sub-solar temperature. Error bars on the modeled diameters and visual albedos were determined for each object by running 20 Monte Carlo trials that varied the objects' H value and the *WISE* magnitudes within their measurement uncertainties using Gaussian probability distributions. The orbital elements a, e, and i, and the NEATM fit results are shown in Table 4 for the *WISE*-observed Centaurs and SDOs. Table 4 also lists the additional eight objects from S08 that were not covered by the *WISE* observations, but have measured $B-R$ colors. The fifth and last columns indicate special details of the thermal model fits and processing. The last column indicates whether the object was discovered by *WISE* (indicated by "D" in the last column), was detected in the WMOPS processing (indicated by "Y"), or was found in subsequent stacking ("N"). Note that an "X" in the last column refers to elements from the S08 results. The entries are listed in categories of Centaurs, in order of perihelion distance q, and SDOs, in order of aphelion distance Q. The first 14 entries in the table are the previously mentioned Satyr objects. The "NEATM fits comment" column indicates whether a fixed beaming parameter η was used for the conditions of the thermal fit. In most cases where there was significant $W3$ and $W4$ signal, η was fit as a free parameter in the modified NEATM model as implemented using the same method described in Grav et al. (2011, 2012a, 2012b), Mainzer et al. (2011b, 2011c), and Masiero et al. (2011). Cases for which η could be fit as a free parameter are labeled "Free" in the fit comments column in Table 4. However, in cases where the freely varying η fit returned non-physical values, i.e., $\eta < 0.5$ (Lebofsky & Spencer 1989; Harris 1998), a fixed η value of 0.8 was used if there were no NEATM fits in S08 or S12 with freely fit η values. An η value of 0.8 was chosen since this was near the mean of the η values found for the freely varying η thermal fits. These cases are listed as "fixed $W3$, $W4$". Instances of "fixed $W3$" or "fixed $W4$" are cases where only a single thermal band was utilized in the fit. Note that the detection for 2010 BL_4 was marginal (3.9σ) and only in $W4$. Also, note that the diameter fit for (10199) Chariklo was smaller than in S08 even though the signal was strong in $W3$ and $W4$. However, if a fixed η value of ~1.2 is used, similar to that found by S08, the derived diameter, 273 ± 100 km, and albedo, 0.04 ± 0.04, values are consistent with the S08 values of 257 ± 13 km and 0.06 ± 0.01. The diameters for (127546) 2002 XU_{93}, 192 ± 50 km, and (42355) Typhon, 170 ± 50 km, were consistent with those found in S12, when utilizing the same values of η, since both bodies were detected only in $W4$. Finally, it is likely that Chiron was weakly active during its observation, and the implications for Chiron's activity will be discussed in Section 3.

Table 4
NEATM Model Fits to *WISE* Flux Measurements

Object[a]	Diam	σ-Diam	Albedo	σ-Albedo	η	$\sigma-\eta$	NEATM Fit Comments	e	a	i	q	T_N	WMOPS-observed?
Centaurs													
"Satyr" Centaurs, 5.5 AU $< a <$ 30.1, $q <$ 5.2													
K08J14S	14.5	1.8	0.044	0.019	1.046	0.186	Free	0.742	11.65	26.0	3.0	3.28	N
K10CE0R	7.5	1.4	0.020	0.01	1.111	0.283	Free	0.408	5.62	74.7	3.32	5.67	D,Y
K10H20U	10.513	1.1	0.101	0.024	0.976	0.162	Free	0.2719	5.8452	22.43	4.2558	4.33	D,Y
K10L61G	0.89	0.19	0.089	0.056	1.00	0.400	Free	0.8078	7.1115	123.7	1.367	3.97	D,Y
K10O01R	3.25	0.64	0.055	0.013	0.831	0.146	Free	0.9245	27.188	143.8	2.0516	1.13	D,Y
K10OA1M	3.12	0.17	0.029	0.005	1.054	0.105	Free	0.9193	26.401	118.7	2.129	1.12	D,Y
K10P58O	8.88	0.63	0.035	0.007	0.915	0.093	Free	0.6594	8.8008	121.1	2.9979	3.28	D,Y
X0759	11.8	0.4	0.097	0.017	0.823	0.046	Free	0.563	8.12	170.4	3.5	4.29	N
Centaurs, 5.5 AU $< a <$ 30.1, $q >$ 5.2													
10199	226.1	29.3	0.075	0.015	1.009	0.049	Free	0.170	15.73	23.4	13.1	0.86	N
167P	66.17	22.9	0.053	0.019	0.8	0.360	Fixed η W4	0.2700	16.141	19.13	11.784	0.54	N
2060	201.2	62.4	0.110	0.052	0.8	0.320	Fixed η W3, W4	0.3792	13.670	6.9	8.486	3.29	N
29P	46.	13.	0.033	0.015	0.64	0.29	Free	0.044	5.998	9.38	5.723	4.15	N
31824	57.0	15.9	0.050	0.028	0.8	0.272	Fixed η W4	0.3835	11.788	5.24	7.267	2.79	N
32532	86.5	1.9	0.059	0.013	1.325	0.049	Free	0.197	10.663	20.3	8.561	3.70	N
52872	36.0	1.2	0.058	0.02	0.97	0.06	Free	0.306	8.34	15.66	5.792	3.93	Y
54598	187.5	15.5	0.050	0.019	1.0	0.09	Free	0.200	16.561	20.7	13.256	1.93	N
55576	100.9	40.1	0.180	0.135	0.8	0.418	Fixed η W4	0.392	24.99	13.3	15.192	0.87	N
60558	59.	4.	0.077	0.015	0.67	0.07	Free	0.457	10.71	4.34	5.81	1.87	Y
95626	230.5	87.50	0.053	0.030	0.8	0.343	Fixed η W4	0.217	23.024	15.0	17.991	1.67	N
C0061	82.0	8.4	0.072	0.032	0.851	0.126	Free	0.473	20.7	19.8	10.92	0.08	N
D6204	118.0	32.8	0.046	0.029	1.0	0.357	Fixed η W4	0.261	20.22	11.2	14.95	2.56	N
E5486	20.8	7.2	0.215	0.123	0.8	0.395	Fixed η W3, W4	0.532	17.637	3.8	8.258	0.96	N
E8975	37.7	10.5	0.041	0.014	0.703	0.186	Free	0.677	28.9	12.6	9.33	2.20	N
K07VU5H	23.8	8.0	0.070	0.036	0.8	0.384	Fixed η W3, W4	0.667	24.606	6.2	8.188	−0.09	N
K08H21Y	24.0	1.5	0.044	0.010	1.22	0.094	Free	0.507	10.96	12	5.41	1.81	N
K10B04L	15.7	3.2	0.114	0.052	0.8	0.333	Fixed η W4	0.5393	18.612	20.81	8.573	1.74	N
K10E65S	26.9	7.9	0.049	0.024	0.8	0.28	Fixed η W3, W4	0.556	21.348	10.4	9.47	2.14	N
K10F92H	28.0	0.6	0.047	0.007	0.730	0.023	Free	0.763	24.4	61.9	5.785	0.10	D,Y
K10R64M	21.0	2.0	0.159	0.048	0.85	0.144	Free	0.685	19.57	27.	6.16	1.82	N
K10T00H	69.9	24.2	0.078	0.033	0.8	0.363	Fixed η W4	0.3254	18.659	26.69	12.587	0.50	N
K11M04M	63.7	6.2	0.083	0.024	0.841	0.119	Free	0.482	21.51	100.4	11.1	−0.03	N
O8835	78.44	22.63	0.046	0.018	0.8	0.357	Fixed η W3, W4	0.463	22.288	36.3	11.961	2.87	N
P0112	38.9	3.5	0.185	0.046	0.661	0.094	Free	0.316	12.6	19.46	8.62	1.21	D,Y
S1371	58.0	4.2	0.120	0.027	0.586	0.061	Free	0.311	14.786	27.1	10.18	2.99	N
U9139	39.1	15.7	0.139	0.058	0.8	0.456	Fixed η W4	0.3779	15.920	31.57	9.903	2.90	N
U9737	17.7	1.5	0.074	0.021	0.800	0.110	Free	0.439	10.99	6.0	6.2	2.49	N
V0071	110.06	30.82	0.121	0.037	0.8	0.324	Fixed η W4	0.5658	29.902	19.67	12.984	−0.12	N
W8884	44.2	3.8	0.083	0.021	0.748	0.103	Free	0.324	13.5	24.8	9.13	2.98	D,Y
X2685	33.0	2.8	0.078	0.018	0.739	0.095	Free	0.446	12.7	23.3	7.0	1.23	N
Y2842	67.1	1.0	0.062	0.012	0.839	0.012	Free	0.443	11.7	105.0	6.49	1.46	Y
Y6889	23.2	9.5	0.062	0.049	0.8	0.389	Fixed η W3	0.4483	10.890	19.88	6.008	2.53	Y
Scattered disk objects													
42355	192.	50.	0.05	0.03	1.48	0.4	Fixed η W4	0.535	37.633	2.4	17.516	2.22	N
C7546	170.	50.	0.04	0.03	1.1	0.4	Fixed η W4	0.6858	66.784	77.90	20.984	−0.99	N
CK11K36P	55.1	19.4	0.101	0.062	0.8	0.4	Fixed η W4	0.875	38.93	18.98	4.88	1.75	N
K05VB9J	28.5	6.9	0.126	0.060	0.8	0.30	Fixed η W4	0.6791	35.104	6.954	11.264	−0.50	N
K10BB8K	46.4	1.8	0.068	0.013	0.821	0.043	Free	0.986	446.8	143.9	6.105	0.34	D,Y
K10G64W	6.42	0.38	0.047	0.012	0.795	0.075	Free	0.9416	63.459	105.3	3.7078	0.93	D,Y
K10GE7W	15.9	0.7	0.037	0.006	0.869	0.056	Free	0.973	199.3	99.7	5.38	0.80	D,Y
K10JC4H	7.04	0.74	0.052	0.024	0.959	0.164	Free	0.9694	85.344	53.37	2.6132	0.18	D,Y
K10K07W	4.87	0.22	0.047	0.011	0.75	0.06	Free	0.9684	81.000	147.1	2.5615	0.62	D,Y
K10W09G	112.7	61.9	0.074	0.080	0.8	0.423	Fixed η W4	0.6511	53.747	70.21	18.753	0.68	N
X6756	44.2	8.0	0.057	0.030	0.661	0.168	Free	0.968	294.0	140.8	9.417	1.58	D,Y
Supplemental data													
NEATM fits from Stansberry et al. (2008)													
5145	*98.*	*25.*	*0.16*	*0.06*	*1.2*	*0.35*	*S08 Fit, 24 μm*[b]	*0.571*	*20.25*	*24.71*	*8.69*	*0.84*	*X*
7066	*60.*	*15.*	*0.06*	*0.04*	*1.2*	*0.35*	*S08 Fit, 24 μm*	*0.524*	*24.83*	*15.63*	*11.81*	*-0.31*	*X*
8405	*85.*	*12.*	*0.05*	*0.02*	*0.7*	*0.2*	*S08 Fit, 2-band*	*0.622*	*18.16*	*17.61*	*6.86*	*0.61*	*X*

Table 4
(Continued)

Object[a]	Diam	σ-Diam	Albedo	σ-Albedo	η	$\sigma-\eta$	NEATM Fit Comments	e	a	i	q	T_N	WMOPS-observed?
							Centaurs						
10370	*70.5*	*19.*	*0.06*	*0.04*	*1.2*	*0.35*	*S08 Fit, 24 μm*	*0.249*	*25.11*	*4.14*	*18.86*	*1.23*	*X*
31824	*41.*	*8.*	*0.06*	*0.04*	*1.2*	*0.35*	*S08 Fit, 24 μm*	*0.414*	*12.74*	*5.59*	*7.46*	*3.53*	*X*
52975	*62.*	*16.*	*0.12*	*0.06*	*1.2*	*0.35*	*S08 Fit, 24 μm*	*0.384*	*26.41*	*12.62*	*16.26*	*2.65*	*X*
63252	*34.*	*7.*	*0.04*	*0.02*	*1.2*	*0.35*	*S08 Fit, 24 μm*[b]	*0.298*	*9.79*	*12.47*	*6.87*	*2.83*	*X*
83982	*59.*	*13.*	*0.11*	*0.07*	*1.2*	*0.35*	*S08 Fit, 24 μm*	*0.274*	*19.34*	*12.78*	*14.04*	*0.06*	*X*

Notes.
[a] Object name in packed-provisional format (http://www.minorplanetcenter.org/iau/info/PackedDes.html). T_N refers to the Tisserand Parameter for Neptune.
[b] Listed diameters, albedos and η, along with their uncertainties, are from S08 (italicized entries). The 24 μm fits used fixed $\eta = 1.2 \pm 0.35$ while the two-band fits were from flux at 24 μm and 70 μm.

3. DISCUSSION

3.1. Albedos, Diameters, and Orbital Elements

We searched our albedo and diameter data for relations based on dynamical properties, with the major caveat that we have not accounted for sample biases that derive from the means by which the objects were detected either by WMOPS or by ground-based visible light surveys. These survey biases can have strong effects on the relationship between these quantities in the observed sample, and caution must be used when interpreting the results without accounting for them. We find no significant relation between size, eccentricity, albedo, or semi-major axis. As stated before, Figure 1 shows only the obvious trends imposed by our detection thresholds. Figure 2 seems at first to indicate that the brightest objects are concentrated at lower inclinations. However, this could as easily be the result of low-number statistics for high-inclination objects, because the ground-based visible surveys that discovered more than half of the objects in our sample do not survey at high inclinations, and so were less likely to find them. Also, high inclination populations may be comprised of objects with cometary origins and surfaces, which have been found to be dark (Fernández et al. 2013). While *NEOWISE* has been shown to be equally sensitive to low and high albedo objects (Mainzer et al. 2011b; Grav et al. 2011, 2012a) and sensitive to high inclination objects (by virtue of being an all-sky survey), about a third of our sample consists of objects detected by stacking on predicted positions of objects discovered by ground-based visible surveys. These surveys are considerably less likely to discover low albedo objects. The dynamical properties investigated also include the Tisserand-parameter relative to Jupiter (T_J), or Neptune (T_N), which is defined as

$$T_{J,N} = \frac{a_{J,N}}{a} + 2\sqrt{\frac{a}{a_{J,N}}(1-e^2)\cos i}, \quad (2)$$

where $a_{J,N}$ is the semi-major axis of Jupiter or Neptune, and a, e, and i are the semi-major axis, eccentricity and inclination of the object. Objects with $T_J < 3$ are considered good candidates for bodies with cometary origins, since most JFCs have $2 < T_J < 3$, and longer period comets have $T_J < 2$ (Levison 1996). Figure 3 is consistent with both the presence of bodies of cometary origin and a possibly significant selection bias, as the low T_J region of the figure tends to be devoid of the higher-albedo objects. These figures indicate that, because the survey biases of the infrared-selected WMOPS-detected sample and the optically selected stacked sample are quite different, care must be taken when extrapolating the results from this observed sample to the populations of Centaurs, SDOs, and Satyrs as a whole. The process of accounting for these survey biases will be the subject of future work. The collective albedos for the Centaurs yield a mean value of 0.08 ± 0.04, which is identical for the SDOs as well. The mean albedo of the Satyr sub-population of Centaurs is

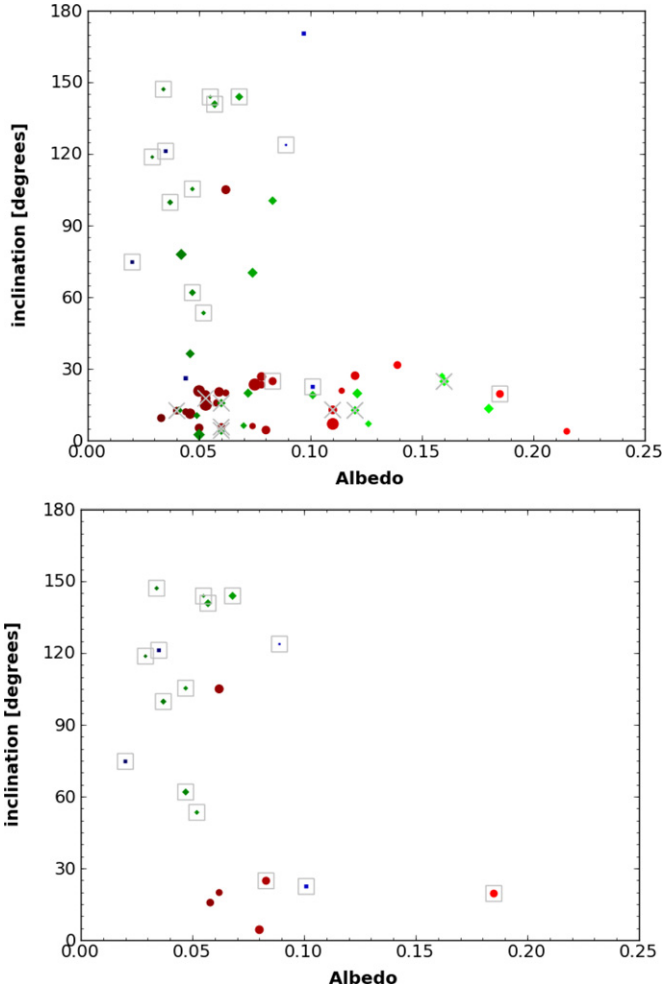

Figure 2. Albedo and orbital inclination, i. The symbols are as in Figure 1, with the log value of the fitted diameter represented by the size of the symbol, and the relative visual-band albedo shown approximately as the darkness of each symbol. The inclination of the populations are shown for the entire sample (top) and the WMOPS-detected sub-sample (bottom). Comparison between the top and bottom panels demonstrates the possible selection bias with respect to inclination that may be extant in ground-based surveys.
(A color version of this figure is available in the online journal.)

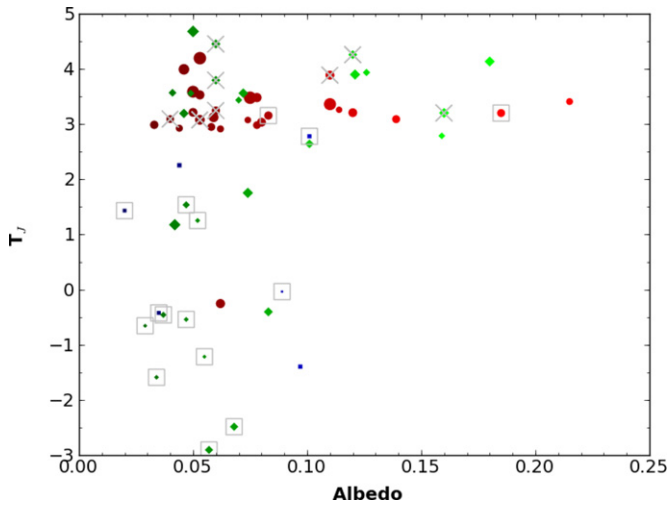

Figure 3. T_J, the Tisserand parameter (relative to Jupiter) versus the derived albedos. The symbols are as in Figure 1, with the log value of the fitted diameter represented by the size of the symbol, and the relative visual-band albedo shown approximately as the darkness of each symbol. Note that the low T_J region of the figure tends to be devoid of the higher-albedo objects, but it is unclear whether this is owing to selection bias of optically selected objects superimposed on objects discovered in the thermal IR.

(A color version of this figure is available in the online journal.)

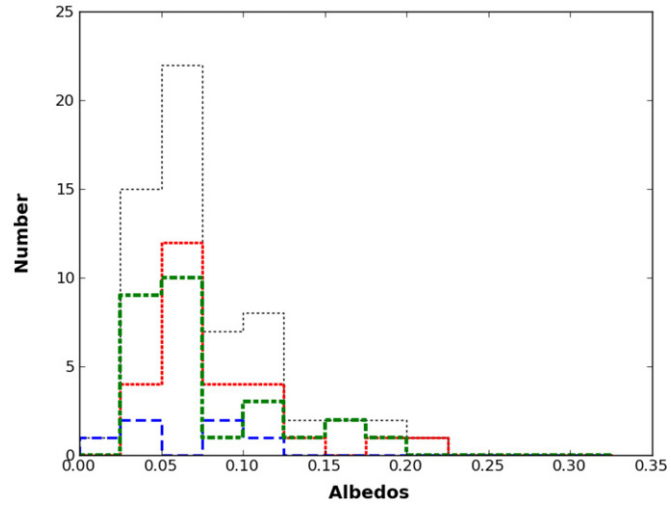

Figure 4. Histogram of albedos for our total sample (black dotted), Centaurs (red dotted), SDOs (green dot-dashed), and the Satyrs (blue dashed). No particular groupings of albedo with respect to these object classifications are separable by number alone.

(A color version of this figure is available in the online journal.)

slightly darker, 0.06 ± 0.03, but the difference is not statistically significant, and falls within the collective mean of the combined SDO and Centaur sample of 0.08 ± 0.04 (Figure 4). These values for p_V overlap the average $p_V \sim 0.07$ value reported for the samples of Centaurs and SDOs in S08 and S12.

3.2. Size–Frequency Distributions

The biased diameters present sufficient first-order statistics for derivation of cumulative size frequency distributions (SFDs; cf. Colwell 1993) for the Centaurs, SDOs and combined samples. Taking the results for all objects, regardless of their distance, we find shallow distributions for the number of these

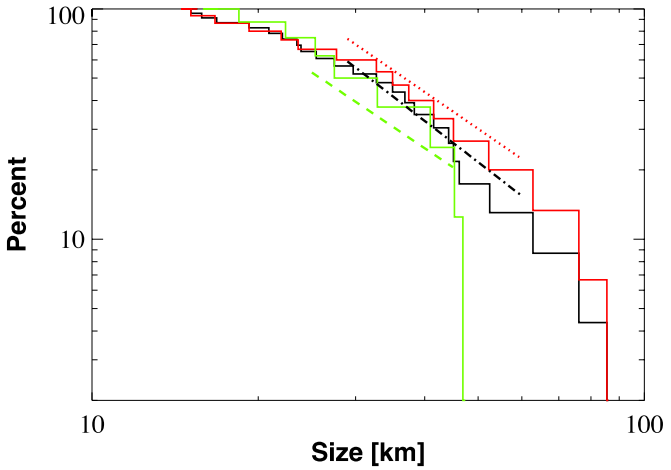

Figure 5. Cumulative size frequency distribution (SFD) of the Centaurs (red) and SDOs (green). The black line indicates the total SFD of the entire sample. The dashed lines indicate the fitted SFD power-law relation for sub-samples of the population less-affected by distance bins (see text), but the power-law distributions of the underlying sample await debaising.

(A color version of this figure is available in the online journal.)

bodies with diameter $d > D$,

$$N(d > D) \sim D^{-\alpha}$$

with power law indices $\alpha \sim 1$, i.e., SFDs dominated by the sensitivity bias (Figure 5). If, however, we select objects detected between 5 and 10 AU, where the sensitivity gradient is less extreme (and dominated by the $W4$ response alone), and with diameters greater than 20 km, we find SFDs of $\alpha = 1.7 \pm 0.2$ for the Centaur and $\alpha = 1.6 \pm 0.3$ for the SDO samples. We also find $\alpha = 1.8 \pm 0.2$ for the combined sample. These values roughly agree with earlier estimates for the Centaurs ($\alpha \sim 2.0$; Jedicke et al. 2002). These power law values also compare favorably with the SDF for JFCs of 1.92 ± 0.2 found by Snodgrass et al. (2011). However, these index values are difficult to interpret without proper de-biasing, which may greatly affect the values. For example, objects at similar distances discovered at visual magnitudes may have higher albedo than those discovered in the thermal IR. In turn, these bodies may have smaller diameters on average, weighting the SFDs toward the smaller-size end and steepening the slope.

3.3. Colors and Albedos

We have found evidence for a correlation between color and surface reflectance in the observed sample. Previous work (cf. Peixinho et al. 2012; Tegler et al. 2008, and references therein) has shown the Centaurs to be divided into two color sub-classes. Most objects tend to have $B-R$ colors closer to the solar value of 1.19 mag (Livingston 2000), i.e., near-neutral reflectance, with $B-R$ colors <1.4 mag. A smaller group has redder colors with $B-R$ in excess of 1.4 mag, clustering with values near $\sim$1.85 mag. With the limited number of centaur albedos available from S08, Tegler et al. (2008) suggested a possible correlation between $B-R$ colors and surface albedo at the 2σ level based on 15 objects.

We conclude that this correlation exists using a sample of 41 objects with color and albedo information available, including the eight additional objects from S08 with measured colors, but not observed by *WISE* (Figure 6). As a check, we divided our sample into $B-R < 1.4$ mag ("near-neutral" reflectance, or

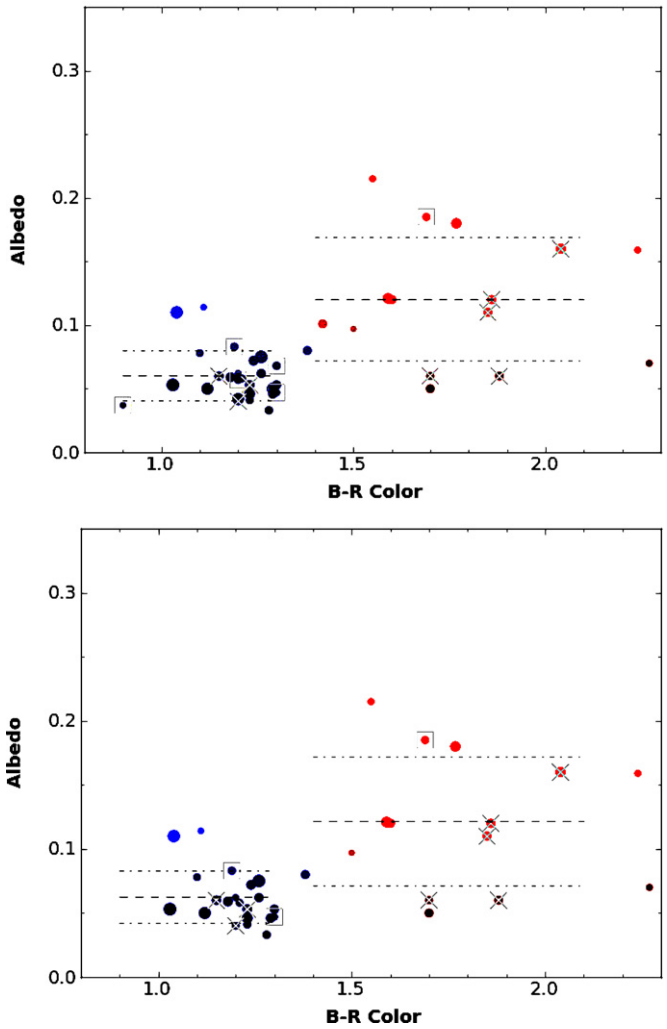

Figure 6. The albedos vs. $B-R$ colors of the total sample (top), and Centaur and "Satyr" populations (bottom). The red group ($B-R > 1.4$) is indicated by the red symbols and the blue ($B-R < 1.4$) by the blue symbols. The mean and standard deviation of each sub-sample are indicated by the dashed and dot-dashed lines, respectively.

(A color version of this figure is available in the online journal.)

"bluer," group) and $B-R > 1.4$ mag ("red" group; cf. Tegler et al. 2008), and ran a two-set Kolmogorov–Smirnov test (Press et al. 1992) to determine the probability that the bluer and red surface sub-populations represented different populations with respect to albedo also. With a 99.95% confidence, the two subclasses were found to be different. The bluer color group had a mean albedo of 6% ± 2%, while that of the redder color group was 12% ± 5%. On average, the redder group had a higher albedo, and also a wider distribution in color. It is also worth noting that the bluer group is closer both in color and albedo to those of cometary nuclei (Fernández et al. 2002, 2013), so that it seems plausible that a direct link between comets and the bluer subclass of Centaurs exists.

3.4. Beaming Parameters

Further evidence of the link between comets and Centaurs may be indicated by the distribution of beaming parameters (Figure 7). The beaming parameter, or η, is a value that accounts for deviations of the temperature distribution from instantaneous thermal equilibrium (cf. Harris & Lagerros 2002; Harris 1998). A body with a low thermal inertia has an η value

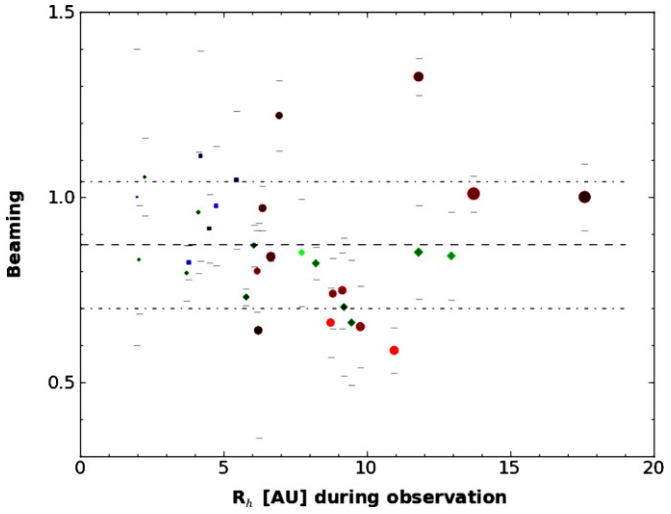

Figure 7. The beaming parameter (η) derived from unconstrained NEATM fits of objects with $W3$ and $W4$ signal. The mean and standard deviation of η for the entire sample are indicated by the dashed and dot-dashed lines respectively. The means and distributions of the separate Centaur, SDO, and "Satyr" populations agree with in the total sample.

(A color version of this figure is available in the online journal.)

close to 1. Since all objects had H_V estimates (Section 2.1), the beaming parameter was fit for all objects with significant $W3$ and $W4$ signal. Those with successful beaming parameter fits are labeled as "Free" in the fits comments column in Table 4. The distribution of the η values from fits of beaming parameter values for objects with significant signal at two or more wavelengths is plotted in Figure 7. The mean value for the total sample and the Centaurs, $\eta = 0.9 \pm 0.2$, is identical to those found for comets (Fernández et al. 2013; Bauer et al. 2012b), including the dispersion as reflected by the standard deviation. For the SDOs, the mean value of $\eta = 0.83 \pm 0.10$ lies within the dispersion of the Centaur average beaming parameters. Similarly, the red ($\eta = 0.73 \pm 0.11$) and bluer ($\eta = 0.87 \pm 0.18$) Centaur beaming parameters overlap statistically.

3.5. Chiron and the Active Centaurs

Four Centaurs with confirmed observations of activity were observed by the *WISE* spacecraft: 174P/Echeclus, C/2010 KW_7, 95P/Chiron, and 29P/Schwassmann-Wachmann 1. Comet 29P/SW1 was active at the time, and a detailed analysis of the 29P observations is the subject of another paper. We present here a diameter value of 46 ± 13 km for 29P's nucleus from a preliminary analysis (Fernández et al. 2012) using the extraction technique described in Bauer et al. (2012a), which is consistent with the value of 54 ± 10 km from Stansberry et al. (2004). Our fitted value for Centaur 174P/Echeclus has a diameter of 59 ± 4 km within 1.7σ of that derived in S08, 84 ± 15 km. We derived an albedo for 174P of 0.08 ± 0.02, nearly twice that found by S08 (0.04 ± 0.02). Activity in 174P was previously detected at wavelengths of 24 and 70 μm using *Spitzer* (Bauer et al. 2008). There was no indication of activity for 174P in the *WISE* images or reported in S08, though it cannot be completely ruled out. C/2010 KW7, with a diameter of 6 ± 1 km based on the NEATM thermal fit, did not show any signs of activity until after its discovery by *NEOWISE* (cf. Scotti & Williams 2010).

Chiron may have been active at the time of the *WISE* observations, but the *WISE* data are consistent with no or low

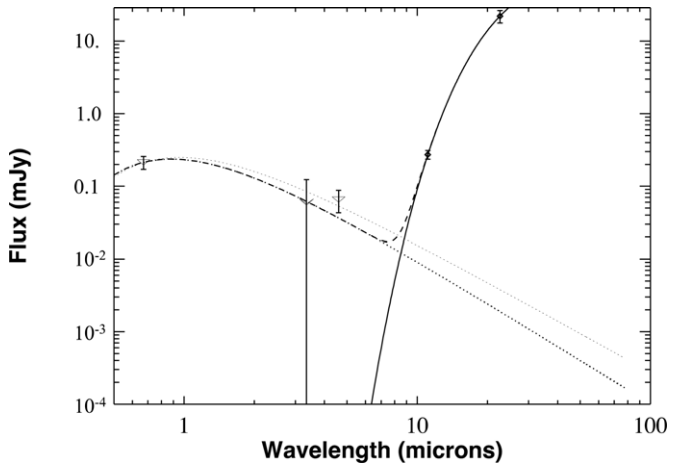

Figure 8. Thermal black body fit to the *WISE* 2010 May 22 *W*3 and *W*4 photometry of the coma and nucleus signal of (2060) Chiron, and the *W*2 infrared excess, for an 11 arcsec aperture radius. The effective temperature for the thermal fit is 101 K. The 1σ upper bound for Chiron's *W*1 flux is also shown at 3.4 μm. The dotted lines represent the reflected-light signal based on the observed visual-band brightness of the comet taken on the same UT date and extrapolated using an assumed dust particle-size distribution for a dust particle size distribution power-law of -3.0 (see text; bold dotted line) and with a reddening law based on Jewitt & Meech (1986; faint dotted line). The combined thermal and reflected light signal for the case without the reddening law is indicated by the dashed line.

activity. The diameter derived from the adapted NEATM thermal fits for the Chiron data (201 $\pm$ 62 km) is in line with other nucleus size estimates such as in S08 (233 $\pm$ 15 km) and including that from a stellar occultation (180 $\pm$ 14; Bus et al. 1996). However, magnitudes at visual wavelengths reported at or around the time of the *NEOWISE* observations at the MPC, and our own observations, were brighter than those expected for a bare nucleus. We observed Chiron on 2010 May 22 from the Palomar Transient Factory's 48 inch telescope (PTF; cf. Law et al. 2009; Waszczak et al 2013; Ofek et al. 2012a, 2012b) and found an *R*-band magnitude (m_R) = 17.86 $\pm$ 0.03. For a bare nucleus of $\sim$200 km diameter with $\sim$15% reflectance (Fernández et al. 2002) and an IAU phase curve slope parameter of $G = 0.15$ (cf. Bowell et al. 1989), we derive $m_R \sim 18.2$. Our measured magnitude is thus consistent with excess brightness caused by activity at the $\sim$0.3 mag level. Comet dust is usually red (Jewitt & Meech 1986), but in the case of Chiron, the coma is neutral (Bauer & Meech 1997), which can be explained by the presence of small grains (Meech et al. 1997). If the excess brightness in the PTF observations was caused by mostly small-grained dust (cf. Meech et al. 1997; Bauer & Meech 1997), the excess would not be readily apparent at the *W*3 and *W*4 wavelengths, as shown below.

We provide a fit to the flux data using the method applied to 67P/Churymov-Gerasimenko (Bauer et al. 2012a), with the visual-band constraint provided by the PTF data, shown in Figure 8. We assume an $\alpha = 3$ dust particle size frequency distribution (DPSFD; cf. Fulle 2004), with both a neutral-reflectance and a reflectance reddening law based on Jewitt & Meech (1986) averaged out to 3.5 μm. A value of α near 3 would be consistent with common cometary DPSFDs, but may overestimate the dust flux at *W*1 and *W*2 for Chiron, possibly owing to an over-abundance of smaller grains. The case for the presence of small grains is possibly strengthened by the temperature fits of 101 $\pm$ 5K, well in excess of the 69 K black-body temperature, but nearly matching the sub-solar-point temperature of $\sim$98 K for $R_h \sim 16.3$ AU. Higher temperature fits to dust coma in excess of black body and sub-solar-point temperatures have been found to be consistent with the dominance of small dust grains in the coma (cf. Lisse et al. 1998; Reach et al. 2000), owing to super-heating and the presence of silicate emission at $\sim$10–12 μm. We find a weak *W*2 signal that is in slight excess of the dust signal that can accommodate CO or CO_2 production rates of 1×10^{28} and 1×10^{27} molecule s^{-1}, respectively (1σ upper limits; Bauer et al. 2012a; Pittichová et al. 2008). However, the excess 4.6 μm flux is greater than the predicted dust and measured nucleus signal at barely the 1σ level (Figure 8), and may as likely be caused by dust scattering or other effects. It is therefore not considered a reliable detection of either species.

4. CONCLUSIONS

We find 52 Centaur and SDO objects in the *WISE* data. Thermal fits yield diameters and albedos for these objects reported in Table 4. We combine known diameters, albedos, and colors from Stansberry et al. (2008) and Tegler et al. (2008) with the *WISE* data and our own color photometry obtained from ground-based observations (Table 2), and find that red and blue Centaurs reflect different populations with respect to albedo with a 99.95% confidence. Blue objects have mean albedos of 0.06 $\pm$ 0.02 and redder objects have mean albedos of 0.12 $\pm$ 0.05. NEATM thermal fits yield mean beaming parameters over the entire sample of 0.89 $\pm$ 0.17, similar to those reported for comet populations, and are consistent with low thermal-inertia surfaces. Cumulative SFDs indicate power law slope values agree similar to earlier estimates for the Centaurs and for the JFCs, with $\alpha \sim 1.7 \pm 0.2$. However, this sample is not debiased, so the SFDs are probably not representative of the general population, given the various selection effects at work.

This publication makes use of data products from the *Wide-field Infrared Survey Explorer*, which is a joint project of the University of California, Los Angeles, and the Jet Propulsion Laboratory/California Institute of Technology, funded by the National Aeronautics and Space Administration. This publication also makes use of data products from *NEOWISE*, which is a project of JPL/Caltech, funded by the Planetary Science Division of NASA. This material is based in part upon work supported by NASA through the NASA Astrobiology Institute under Cooperative Agreement No. NNA09DA77A issued through the Office of Space Science. R. Stevenson is supported by the NASA Postdoctoral Program, and E. Kramer acknowledges her support through the JPL graduate internship program. Data were based in part on observations obtained at the Hale Telescope, Palomar Observatory, as part of a collaborative agreement between the California Institute of Technology, its divisions Caltech Optical Observatories, and the Jet Propulsion Laboratory (operated for NASA). Also, this work is based in part on observations obtained at the Southern Astrophysical Research (SOAR) telescope, which is a joint project of the Ministério da Ciência, Tecnologia, e Inovação (MCTI) da República Federativa do Brasil, the U.S. National Optical Astronomy Observatory (NOAO), the University of North Carolina at Chapel Hill (UNC), and Michigan State University (MSU), with time allocated through NOAO. We thank the anonymous reviewer for the very helpful comments of manuscript drafts.

REFERENCES

A'Hearn, M. F., Millis, R. L., Schleicher, D. G., Osip, D. J., & Birch, P. V. 1995, Icar, 118, 223

Barucci, M. A., Brown, M. E., Emery, J. P., & Merlin, F. 2008, in The Solar System Beyond Neptune, ed. M. A. Barucci, H. Boehnhardt, D. P. Cruikshank, & A. Morbidelli (Tucson, AZ: Univ. Arizona Press), 143

Bauer, J. M., Choi, Y.-J., Weissman, P. R., et al. 2008, PASP, 120, 393

Bauer, J. M., Kramer, E., Mainzer, A. K., et al. 2012a, ApJ, 758, 18

Bauer, J. M., Kramer, E., Stevenson, R., et al. 2012b, *WISE*/*NEOWISE* Comets: Nucleii and CO/CO2 Emission, AAS/Division for Planetary Sciences Meeting Abstracts 44, #514.08

Bauer, J. M., Mainer, A. K., Grav, T., et al. 2012c, ApJ, 747, 49

Bauer, J. M., & Meech, K. J. 1997, M&PS, 32, 10

Bauer, J. M., Meech, K. J., Fernández, Y. R., et al. 2003, Icar, 166, 195

Bauer, J. M., Meech, K. J., Fernandez, Y. R., Farnham, T. L., & Roush, T. L. 2002, PASP, 114, 1309

Bauer, J. M., Walker, R. G., Mainer, A. K., et al. 2011, ApJ, 738, 171

Bessell, M. S. 1990, PASP, 102, 1181

Bowell, E., Hapke, B., Domingue, D., et al. 1989, in Asteroids II (Tucson, AZ: Univ. Arizona Press), 524

Brown, M. E. 2000, AJ, 119, 977

Bus, S. J., Buie, M. W., Schleicher, D. G., et al. 1996, Icar, 123, 478

Colwell, J. E. 1993, in Proc. 24th Lunar and Planetary Science Conf., Power-Law Confusion: You Say Incremental, I Say Differential, Houston, TX, 1993 March 15–19, 325

Cutri, R. M., Wright, E. L., Conrow, T., et al. 2012, Explanatory Supplement to the *WISE* All-sky Data Release 2011, (http://wise2.ipac.caltech.edu/docs/release/allsky/expsup/)

Dailey, J., Bauer, J., Grav, T., et al. 2010, BAAS, 41, 409.04

Davies, J. K., McFarland, J., Bailey, M. E., Marsden, B. G., & Ip, W.-H. 2008, in The Solar System Beyond Neptune, ed. M. A. Barucci, H. Boehnhardt, D. P. Cruikshank, & A. Morbidelli (Tucson, AZ: Univ. Arizona Press), 11

Delsanti, A., & Jewitt, D. 2006, in The Solar System Beyond The Planets, ed. P. Blondel & J. Mason (Berlin: Springer), 267

Delsanti, A., Peixinho, N., Boehnhardt, H., et al. 2006, AJ, 131, 1851

Duncan, M. J., & Levison, H. F. 1997, Sci, 276, 1670

Elliot, J. L., Kern, S. D., Clancy, K. B., et al. 2005, AJ, 129, 1117

Fernández, Y. R., Bauer, J. M., Samarasinha, N. H., et al. 2012, LPICo, 1667, 6378

Fernández, Y. R., Jewitt, D. C., & Sheppard, S. S. 2002, AJ, 123, 1050

Fernández, Y. R., Kelley, M. S., Lamy, P. L., et al. 2013, Icar, in press

Fraser, W. C., & Brown, M. E. 2012, ApJ, 749, 33

Fulle, M. 2004, in Comets II, ed. M. C. Festou, H. U. Keller, & H. A. Weaver (Tucson, AZ: Univ. Arizona Press), 565

Gladman, B., Marsden, B. G., & Vanlaerhoven, C. 2008, in The Solar System Beyond Neptune, ed. M. A. Barucci, H. Boehnhardt, D. P. Cruikshank, & A. Morbidelli (Tucson, AZ: Univ. Arizona Press), 43

Grav, T., Mainzer, A. K., Bauer, J., et al. 2012a, ApJ, 744, 197

Grav, T., Mainzer, A. K., Bauer, J. M., Masiero, J. R., & Nugent, C. R. 2012b, ApJ, 759, 49

Grav, T., Mainzer, A. K., Bauer, J., Masiero, J., et al. 2011, ApJ, 742, 40

Hainaut, O. R., Boehnhardt, H., & Protopapa, S. 2012, A&A, 546, A115

Harris, A. W. 1998, Icar, 131, 291

Harris, A. W., & Lagerros, J. S. V. 2002, in Asteroids III, ed. W. F. Bottke, Jr., A. Cellino, P. Paolicchi, & R. P. Binzel (Tucson, AZ: Univ. Arizona Press), 205

Holman, M. J., & Wisdom, J. 1993, AJ, 105, 1987

Horner, J., Evans, N. W., & Bailey, M. E. 2004, MNRAS, 354, 798

Jedicke, R., Larsen, J., & Spahr, T. 2002, in Asteroids III, ed. W. F. Bottke et al. (Tucson, AZ: Univ. Arizona Press), 71

Jewitt, D. C. 2004, in Comets II, ed. M. C. Festou, H. U. Keller, & H. A. Weaver (Tucson, AZ: Univ. Arizona Press), 659

Jewitt, D. C. 2009, AJ, 137, 4296

Jewitt, D. C., & Kalas, P. 1998, ApJL, 499, L103

Jewitt, D., & Meech, K. J. 1986, ApJ, 310, 937

Kelley, M. S., Fernández, Y. R., Licandro, J., et al. 2013, Icar, 225, 475

Lamy, P. L., Toth, I., Weaver, H. A., et al. 2001, BAAS, 33, 1093

Law, N. M., Kulkarni, S. R., Dekany, R. G., et al. 2009, PASP, 121, 1395

Lebofsky, L. A., & Spencer, J. R. 1989, in Asteroids II, ed. R. P. Binzel, T. Gehrels, & M. S. Matthews (Tucson, AZ: Univ. Arizona Press), 128

Levison, H. F. 1996, in ASP Conf. Ser. 173, Completing the Inventory of the Solar System, ed. T. W. Rettig & J. M. Hahn (San Francisco, CA: ASP), 173

Levison, H. F., & Duncan, M. J. 1997, Icar, 127, 13

Lisse, C. M., A'Hearn, M. F., Hauser, M. G., et al. 1998, ApJ, 496, 971

Lisse, C. M., Bar-Nun, A., Laufer, D., et al. 2013, in The Science of Solar System Ices, ed. M. S. Gutipati & J. Castillo-Rogez (New York: Springer), 455

Livingston, W. C. 2000, in Allen's Astrophysical Quantities, ed. A. N. Cox (New York: Springer), 339

Mainzer, A., Bauer, J., Grav, T., et al. 2011a, ApJ, 731, 53

Mainzer, A., Grav, T., Masiero, J., et al. 2011b, ApJ, 736, 100

Mainzer, A., Grav, T., Masiero, J., et al. 2011c, ApJL, 737, L9

Masci, F. J., & Fowler, J. W. 2009, in ASP Conf. Ser. 411, Astronomical Data Analysis Software and Systems XVIII, ed. D. A. Bohlender, D. Durand, & P. Dowler (San Francisco, CA: ASP), 67

Masiero, J. R., Mainzer, A. K., Grav, T., et al. 2011, ApJ, 741, 68

Meech, K. J., Buie, M. W., Samarasinha, N. H., Mueller, B. E. A., & Belton, M. J. S. 1997, AJ, 113, 844

Nugent, C. R., Mainzer, A., Masiero, J., Grav, T., & Bauer, J. 2012, AJ, 144, 75

Ofek, E. O., Laher, R., Law, N., et al. 2012a, PASP, 124, 62

Ofek, E. O., Laher, R., Surace, J., et al. 2012b, PASP, 124, 854

Ortiz, J. L., Baumont, S., Gutierrez, P. J., & Roos-Serote, M. 2002, A&A, 388, 661

Ortiz, J. L., Gutierrez, P. J., Casanova, V., & Sota, A. 2003, A&A, 407, 1149

Peixinho, N., Delsanti, A., Guilbert-Lepoutre, A., Gafeira, R., & Lacerda, P. 2012, A&A, 546, A86

Pittichová, J., Woodward, C. E., Kelley, M. S., & Reach, W. T. 2008, AJ, 136, 1127

Pravec, P., Harris, A. W., Kuvsnirak, P., Galad, A., & Hornoch, K. 2012, Icar, 221, 365

Press, W. H., Teukolsky, S. A., Vetterling, W. T., & Flannery, B. P. 1992, Numerical Recipes in C. The Art of Scientific Computing (2nd ed.; Cambridge: Cambridge Univ. Press)

Reach, W. T., Sykes, M. V., Lien, D., & Davies, J. K. 2000, Icar, 148, 80

Rousselot, P., Petit, J.-M., Poulet, F., & Sergeev, A. 2005, Icar, 176, 478

Santos-Sanz, P., Lellouch, E., Fornasier, S., et al. 2012, A&A, 541, A92

Schleicher, D. G., Knight, M. M., Farnham, T. L., Schwieterman, E. W., & Christensen, S. R. 2012, BAAS, 44, #514.09

Scotti, J. V., & Williams, G. V. 2010, Minor Planet Electronic Circulars 2010-W20

Sheppard, S. S. 2010, AJ, 139, 1394

Snodgrass, C., Fitzsimmons, A., Lowry, S. C., & Weissman, P. 2011, MNRAS, 414, 458

Stansberry, J., Grundy, W., Brown, M., et al. 2008, in The Solar System Beyond Neptune, ed. M. A. Barucci, H. Boehnhardt, D. P. Cruikshank, & A. Morbidelli (Tucson, AZ: Univ. Arizona Press), 161

Stansberry, J. A., Van Cleve, J., Reach, W. T., et al. 2004, ApJS, 154, 463

Tegler, S. C., Bauer, J. M., Romanishin, W., & Peixinho, N. 2008, in The Solar System Beyond Neptune, ed. M. A. Barucci, H. Boehnhardt, D. P. Cruikshank, & A. Morbidelli (Tucson, AZ: Univ. Arizona Press), 105

Thirouin, A., Ortiz, J. L., Duffard, R., et al. 2010, A&A, 522, A93

Waszczak, A., Ofek, E. O., Aharonson, O., et al. 2013, MNRAS, in press (arXiv:1305.7176)

Werner, M. W., Roellig, T. L., Low, F. J., et al. 2004, ApJS, 154, 1

Wright, E. L., Eisenhardt, P. R. M., Mainzer, A. K., et al. 2010, AJ, 140, 1868